Double time window targeting technique: Real-time DMRG dynamics in the Pariser-Parr-Pople model

Tirthankar Dutta* and S. Ramasesha†

Solid State and Structural Chemistry Unit, Indian Institute of Science, Bangalore 560012, India
(Received 8 March 2010; revised manuscript received 21 May 2010; published 19 July 2010)

We present a generalized adaptive time-dependent density matrix renormalization-group (DMRG) scheme, called the *double time window targeting* (DTWT) technique, which gives accurate results with nominal computational resources, within reasonable computational time. This procedure originates from the amalgamation of the features of pace keeping DMRG algorithm, first proposed by Luo *et al.* [Phys. Rev. Lett. **91**, 049701 (2003)] and the time-step targeting algorithm by Feiguin and White [Phys. Rev. B **72**, 020404 (2005)]. Using the DTWT technique, we study the phenomena of spin-charge separation in conjugated polymers (materials for molecular electronics and spintronics), which have long-range electron-electron interactions and belong to the class of strongly correlated low-dimensional many-body systems. The issue of real-time dynamics within the Pariser-Parr-Pople (PPP) model which includes long-range electron correlations has not been addressed in the literature so far. The present study on PPP chains has revealed that, (i) long-range electron correlations enable both the charge and spin degree of freedom of the electron, to propagate faster in the PPP model compared to Hubbard model, (ii) for standard parameters of the PPP model as applied to conjugated polymers, the charge velocity is almost twice that of the spin velocity, and (iii) the simplistic interpretation of long-range correlations by merely renormalizing the U value of the Hubbard model fails to explain the dynamics of doped holes/electrons in the PPP model.

I. INTRODUCTION

Low-dimensional strongly correlated many-body systems have been in the forefront of both theoretical and experimental researches for many decades, owing to their physics being very different from that of the three-dimensional systems. For example, these materials exhibit the phenomena of spin-charge separation, wherein the spin and charge degrees of freedom of the electron get decoupled from each other and propagate independently with different velocities. From an application point of view also, these materials are in enormous demand. Among the genre of low-dimensional strongly correlated materials, the π-conjugated polymers have attracted huge interest, being potential candidates for various molecular electronic and spintronic applications; examples include the organic light emitting diodes, organic semiconductors and organic thin-film transistors.[1–4] However, spin and charge transport in these materials is still far from well understood because of the strong long-range electron-electron correlations that exist in these systems. Transport is strictly a nonequilibrium phenomena, to understand which, one needs to investigate time evolution of appropriate wave packets in these strongly correlated low-dimensional systems. The density matrix renormalization-group (DMRG) technique advanced by White[5,6] has proved to be a very powerful numerical method for studying large interacting low-dimensional quantum lattice systems. Originally formulated as a ground-state method, this technique has been mostly used for studying static (equilibrium) quantum many-particle phenomena. Later, it was extended to calculate frequency-dependent spectral functions by the correction vector or the Lanczos techniques,[7–14] thereby adapting it to deal with dynamical (equilibrium) many-body phenomena. In this regard, the dynamical DMRG (DDMRG) method[15] turned out to be

the spectral method, best suited for obtaining extremely accurate spectra. However, the DDMRG technique is limited to only one momentum and a narrow frequency range at a time. Constructing an entire spectrum using this method in order to obtain a reasonable grid in frequency and momentum space involves independent runs for each frequency and momentum and is therefore, computationally highly intensive. An alternative route exists for obtaining an entire spectrum in a single run which involves time evolving an appropriate wave packet in real space and time, followed by converting the information from $(\vec{r}, t)$ space to $(\vec{k}, \omega)$ space using double Fourier transform. Quantum dynamics of a wave packet in real space time is needed to obtain the $(\vec{r}, t)$ data, which for large systems was not feasible, until recently. Three of the recent time-dependent DMRG (t-DMRG) techniques are the pace keeping DMRG scheme due to Luo, Xiang, and Wang (LXW),[16] the adaptive t-DMRG method,[17–19] and the time-step targeting (TST) technique due to White.[20] In this paper we present a time-dependent DMRG scheme which is a hybrid of the LXW and TST algorithms. The organization of the paper is as follows: In Sec. I we give an overview of the existing time-dependent DMRG techniques, followed by a detailed discussion of the LXW and TST algorithms in order to compare their strengths and weaknesses. Section II is devoted to a detailed presentation of our algorithm. Section III discusses some numerical issues associated with the DTWT scheme. In Sec. IV we compare the technique with the LXW and TST schemes. In Sec. V we present real-time dynamics of spin-charge separation in regular Pariser-Parr-Pople (PPP) chains using our DTWT algorithm. Section VI provides the summary and conclusions of this work.

Overview of existing time-dependent DMRG methods

The study of out-of-equilibrium phenomena in strongly correlated low-dimensional systems has attained a forefront;

DMRG has played a significant role in this context. Real space-time quantum dynamics using DMRG was introduced by Cazalilla and Marston.[21] They calculated time evolution of one-dimensional systems under the influence of an applied bias. Their approach involved the use of DMRG for constructing the Hilbert space of the Hamiltonian using only the ground state, and subsequently solving the time-dependent Schrödinger equation numerically using the Hamiltonian matrix obtained in a *fixed basis*. Hence, the approach of Cazalilla and Marston is essentially static with respect to the Hilbert space in which time evolution is carried out. It is expected that when the evolving wave function becomes significantly different from the ground state, i.e., "it moves out of the Hilbert space used for time evolution," it will loose accuracy. However, in the systems studied by them, this (expected) loss in accuracy with time did not occur within the time period for which they carried out the time evolution. The drawback of performing time evolution using a fixed DMRG basis is, one needs to keep a substantially large number of the density matrix eigenvectors (DMEVs), m, so that the evolved state is well described by the DMRG basis at large times. Luo, Xiang, and Wang[16] showed an effective way, also known as pace keeping DMRG, to construct DMEV basis for time evolving a wave function over a longer time interval. This is done by constructing a weighted average density matrix from the time-evolved wave functions at discrete time steps $\Delta\tau$ in the time interval $0-T$. Thus,

$$\rho_{L/R} = \text{Tr}_{R/L}\sum_{i=0}^{N_t} \alpha_i |\psi(t_i)\rangle\langle\psi(t_i)|; \quad \sum_i \alpha_i = 1, \qquad (1)$$

where $N_t = \frac{T}{\Delta\tau}$. The weights α_i are taken to be 1/2 for $i=0$ and $\frac{1}{2N_t}$ otherwise. However, their approach suffers from two significant drawbacks. The LXW scheme performs *full* time evolution of the wave function at each infinite DMRG step thereby making it extremely time consuming. In DMRG calculations with multiple target states, truncation error is reduced by keeping the number of DMEVs (m), greater than the number of target states. But in the LXW algorithm, the number of target states N_t [each target state corresponding to $\psi(t_i)$ at time t_i] is usually $\geq m$, thereby decreasing accuracy. Modification of the original LXW scheme in which $\rho_{L/R}$ is obtained as an average in each subinterval Δt, where $\Delta t = p\Delta\tau$, $p \ll N_t$, leads to a decrease in number of target states required, and consequently increases accuracy of the results.[22] In an earlier study, we demonstrated this for $T = 33$ fs, $N_t = 50\,000$, $\Delta\tau = 0.00066$ fs and $p = 200-500$. In fact, the accuracy is not degraded even for $p = 100$. However, our earlier work has shown that this modification works well for nearest-neighbor Hamiltonians like the tight-binding (Hückel) and Hubbard models only. But, in the case of models with long-range interactions, like the PPP Hamiltonian, the above modification fails and we need to average the density matrix over all time steps.

In the context of simulating time evolution of matrix product states (MPS), Vidal developed a novel numerical scheme called the time-evolving block decimation technique.[17] As DMRG is closely related to MPS, this method was immediately utilized by the DMRG community

to develop a very powerful numerical technique called adaptive t-DMRG,[18,19] for studying real-time quantum dynamics in strongly correlated many-particle systems. The key idea of t-DMRG technique is to incorporate the Suzuki-Trotter (ST) decomposition of the time evolution operator $\exp(-i\Delta\tau H)$ into the finite DMRG algorithm. Usually, second-order ST decomposition is used but higher order ST decompositions of the matrix exponential can be employed as well. The second-order Suzuki-Trotter breakup is

$$e^{-i\Delta\tau H} \approx e^{-i\Delta\tau H_A/2}e^{-i\Delta\tau H_B}e^{-i\Delta\tau H_A/2} + O(\Delta\tau^3), \qquad (2)$$

where H_A is the Hamiltonian for the bond connecting sites $(2j-1, 2j)$ and H_B connects sites $(2j, 2j+1)$; $j = 1, 2, \ldots, \frac{N}{2}$, for H_A and $j = 1, 2, \ldots, \frac{N}{2}-1$, for H_B. This breakup leads to grouping of terms such that all terms within H_A or within H_B which commute with each other, leading to high accuracy in the Trotter breakup. A DMRG superblock state, at a particular step n of the finite-system sweep, can be represented as

$$|\psi\rangle = \sum_L \sum_{\alpha_n, \alpha_{n+1}} \sum_R \psi_{L\alpha_n\alpha_{n+1}R}|L\rangle|\alpha_n\alpha_{n+1}\rangle|R\rangle, \qquad (3)$$

where $|L\rangle$ and $|R\rangle$ represent the truncated DMEV basis states of the left and right blocks, and $|\alpha_n\alpha_{n+1}\rangle$ represent the Fock-space states for the two central sites. Thus, an operator ($\hat{A}$) acting on the two central sites can be exactly expressed in the same optimal basis as

$$[\hat{A}\psi]_{L\alpha_n\alpha_{n+1}R} = \sum_{\alpha_n'\alpha_{n+1}'} \hat{A}_{\alpha_n\alpha_{n+1};\alpha_n'\alpha_{n+1}'}\psi_{L\alpha_n'\alpha_{n+1}'R}. \qquad (4)$$

The ST decomposed time evolution operator for the bond connecting sites n and $n+1$ can be applied exactly on the DMRG superblock state at step n of the finite DMRG algorithm. A full finite DMRG sweep corresponds to a time evolution by $2\Delta\tau$ of the full system. In the t-DMRG scheme, two types of errors are involved: (1) the DMRG truncation error and (2) the ST decomposition error, which for second-order decomposition is $O(\Delta\tau^3)$, in each time step. Adaptive t-DMRG based on the Suzuki-Trotter decompositions of the time evolution operator is restricted to nearest-neighbor interactions only since the breakup into H_A and H_B is valid only in this case. Schmitteckert[23] proposed a Krylov space approach for obtaining the exponential time evolution operator. In this method a small matrix representation of the original Hamiltonian, H, is obtained in the basis vectors of the Krylov space, namely, $\{\vec{x}, H\vec{x}, H^2\vec{x}, \ldots, H^{l-1}\vec{x}; \vec{x}$, an arbitrary vector$\}$ for an lth dimensional Krylov space. This permits explicit form of the time evolution operator in a finite optimized basis. He, however, employed the LXW scheme for obtaining the DMRG space spanned by the Hamiltonian.

White proposed a second adaptive approach called the TST technique to circumvent the nearest-neighbor limitation associated with ST breakup.[20] Two key ideas are introduced in this scheme. The first being, there is no conceptual need to have the *same* time step for time evolution and for building the Hilbert space of the evolving wave function. This simply implies that the time scales $\Delta\tau$ on which time evolution is discretized and Δt on which the DMEV basis is adapted,

need not be identical (this is the crucial difference between the LXW and TST schemes). The observation from the work of Cazalilla and Marston that even a static state space remains a good choice for some finite time, implies the choice of $\Delta t > \Delta \tau$. Thus, one can evolve the wave function using any of the non-Trotter methods, the one used by White and Feiguin being fourth-order Runge-Kutta (R-K) technique. Other available methods are the Crank-Nicholson scheme or Krylov-space-based decomposition of the matrix exponential.[24] The second key idea of the TST technique is to adaptively build the Hilbert space representing the time-evolving wave function, at intervals Δt, from the states which are expected to appear in future through time evolution. For this purpose, several DMRG sweeps are carried out at a fixed time t. For each $(L-\alpha_n-\alpha_{n+1}-R)$ configuration during these finite sweeps, a fourth-order Runge-Kutta integration is carried out, and the time-evolved states $|\psi(t+j\Delta t)\rangle$, $j=0,\frac{1}{3},\frac{2}{3},1$ are used to build the reduced density matrices of the blocks using Eq. (1). After sufficient number of sweeps, when the Hilbert space optimally represents the wave function $|\psi(t)\rangle$, final time evolution is performed using a time step $\Delta \tau \approx \frac{\Delta t}{10}$. The new wave function is then used to build the DMEV basis for the next time propagation. Both LXW and the TST techniques are *generalized* adaptive time-dependent DMRG schemes since they can be applied to any Hamiltonian, with arbitrary range (beyond nearest neighbor) of interactions. This flexibility stems from the fact that the time evolution operator is not decomposed using Suzuki-Trotter-type decomposition schemes. In the LXW technique, adaptive construction of the Hilbert space of the time-evolving initial state as well as temporal propagation are performed within the context of infinite DMRG algorithm. On the other hand, TST technique uses the finite DMRG scheme to adaptively update the Hilbert space of the time-evolving wave function as well as propagate it in time. The time steps used for state space updating and time evolution of the wave packet are the same in LXW scheme while they are chosen to be independent in the TST scheme. As stated by White, the time step for basis adaptation (Δt) is larger than that for evolution ($\Delta \tau$).

We have compared the two techniques and have found that, for a given value of m and system size N, LXW scheme besides being comparable in speed with the TST algorithm, is also more accurate. In the LXW scheme, at every system size we need to evolve the wave packet over the entire time period, before getting the DMEV basis for moving to the next system size. In the TST scheme, although we do the time evolution only for the desired finite-system size, we employ a finite DMRG scheme at every time evolution step $\Delta \tau$, which entails large CPU times. The higher accuracy of the LXW scheme arises from the fact that DMEV basis is obtained from a weighted average density matrix, constructed from time-evolved wave packets at all time intervals while in TST scheme the weighted average density matrix is constructed from the wave packets 0, $\frac{\Delta t}{3}$, $\frac{2\Delta t}{3}$, and Δt for each time step of evolution $\Delta \tau$.

If one uses the *window modification* of the LXW technique as proposed by us,[22] thereby decreasing the number of target states, the accuracy as well as computational speed can

be further improved. The above observations leads one to conclude that the LXW technique is superior compared to the TST scheme. However, LXW scheme also suffers from two serious drawbacks: first, LXW method is not *quasiexact* unlike the TST scheme. An approximate DMRG algorithm is quasiexact when the error in the observables is strictly controlled by the truncation error, $\varepsilon = 1.0 - \Sigma_i \rho_i$, ρ_i being the dominant eigenvalues corresponding to the reduced density-matrix eigenvectors which are retained. In case of a quasiexact scheme, the errors in expectation values of the system's properties are either proportional to ε or $\sqrt{\varepsilon}$, that is, $(\langle \hat{O}(t) \rangle_{\text{DMRG}} - \langle \hat{O}(t) \rangle_{exact}) \propto \varepsilon$ or $\sqrt{\varepsilon}$. The infinite-system DMRG technique applied to a finite system is not a quasiexact approximation scheme even though ε goes to zero as m increases. However, in the absence of any metastable ground states and with "sufficient" number of sweeps, the finite-system DMRG algorithm is quasiexact. LXW scheme being an infinite-system DMRG algorithm applied to finite systems is *nonquasiexact*.[20] Second, in case of long-range Coulomb interaction as in the PPP Hamiltonian, our window modification fails, thereby making it necessary to retain all the time-dependent target states. This makes the LXW scheme computationally inefficient. Finally, both the LXW and TST techniques are computationally time consuming. These observations motivated us to develop a real-time evolution method which will have the strengths of both these methods while overcoming their limitations of long computational times and poor accuracy, especially for long-range interacting models.

II. DOUBLE TIME WINDOW TARGETING (DTWT) ALGORITHM

Conceptually, the scheme which we have implemented is a hybrid of the LXW and TST algorithms described in the previous section. These schemes differ from each other mainly in the prescription for constructing the weighted average density matrix. The different schemes are compared schematically in Fig. 1. In the LXW scheme, the weighted average density matrix is obtained from the density matrices of the time-evolved states at all times $(0, T)$ in steps of $\Delta \tau$, the total time interval from $0 \rightarrow T$ being Δt. In the TST scheme, in each time interval Δt, a weighted average density matrix is constructed, typically with the states at the beginning and end of the time interval and at two equidistant intermediate points. The time evolution is carried out with a time step $\Delta \tau$ such that, $\Delta \tau$ is $\sim \frac{\Delta t}{10}$ within the interval. For time evolution over the next time step $\Delta \tau$ to $2\Delta \tau$, the density matrix is constructed using the time interval from $\Delta \tau$ to $(\Delta t + \Delta \tau)$. Besides, in the TST algorithm, unlike in the LXW algorithm, finite DMRG procedure is carried out at each time at which the density-matrix computation is carried out. In the present scheme which we call the DTWT technique, we construct the density matrix over a time interval $2p\Delta \tau$, as a weighted average of the density matrices built at time steps of length $\Delta \tau$, and use the DMEVs from the resulting density matrix to constructing the Hilbert space of the Hamiltonian, for time evolving the desired wave packet from $\Delta \tau$ to $p\Delta \tau$. In this technique, each time interval of length Δt is broken
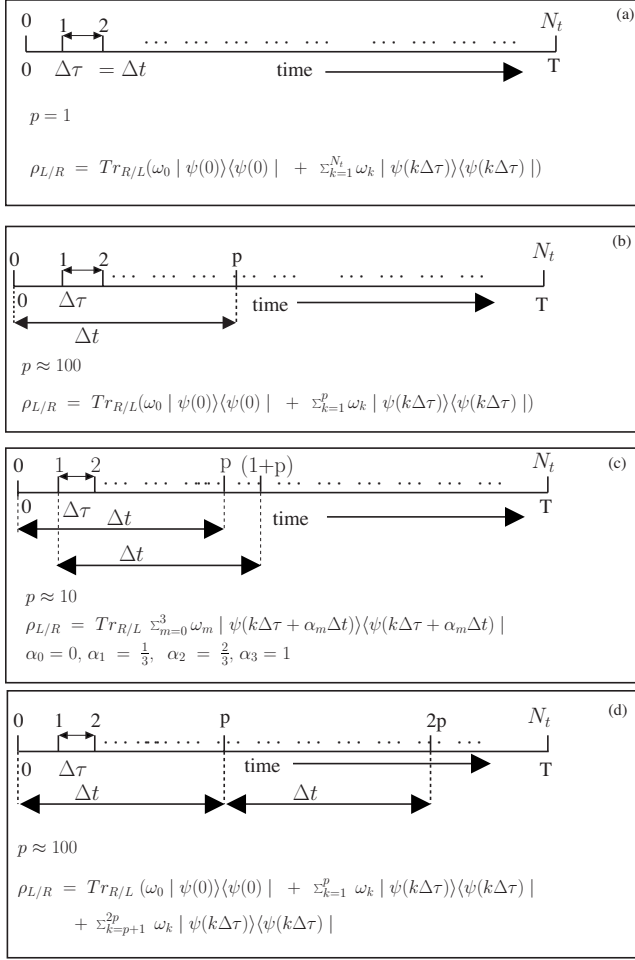
FIG. 1. Pictorial representation of the construction of the time averaged reduced density matrices for left/right block ($\rho_{L/R}$) in the (a) original LXW, (b) modified LXW, (c) TST, and (d) DTWT schemes. In all the schemes, $\Delta\tau = \frac{T}{N_t}$ and $\Delta t = p\Delta\tau$. In the original LXW scheme (a), $\Delta t = \Delta\tau(p=1)$ is used while in our modified LXW scheme (b), $\Delta t = p\Delta\tau$, with $p \approx 100$ is used. In the TST scheme (c), a sliding time window of length Δt is used for updating time step $\Delta\tau(\Delta t \approx 10\Delta\tau)$. In the DTWT method (d), a sliding time window of length $2\Delta t = 2p\Delta\tau$ is used for updating time window of length $\Delta t = p\Delta\tau$, $p \approx 100$. In the last two schemes, finite DMRG procedure is carried out to obtain basis adaptation and time evolution.

into p subintervals of length $\Delta\tau$ such that, while the wave packet evolves by Δt, the basis is adapted over an interval $2\Delta t$. After every time evolution by Δt, the interval is slided by $2\Delta t$ for constructing the Hilbert space for the next time evolution. Thus, approximate future states for a time period $2\Delta t$ are used for evolving the wave packet over a time interval Δt, in steps of $\Delta\tau$. As in the TST scheme, we employ finite procedure to get accurate wave functions in each time interval.

A. Initial wave-packet construction

A conventional infinite DMRG algorithm is carried out to build the system of desired final size on which time evolution is wished to be performed. We wish to study the dynam-

ics of spin and charge transport in a one-dimensional model with long-range interactions. Therefore, the initial wave packet at $t=0$ is formed by annihilating an upspin ($\uparrow$) electron from site 1 of a neutral system in the ground state ($|\psi_{gs}^0\rangle$),

$$|\psi(0)\rangle = a_{1,\uparrow}|\psi_{gs}^0\rangle. \tag{5}$$

Since we are interested in the time evolution of this charged wave packet formed by annihilating an electron in the chain, the Hilbert space formed from the DMEVs of the neutral system alone, would be inappropriate. Hence we construct the half-block density matrices at each system size as a weighted average of the density matrices of the desired wave packet, the neutral ground state, and other relevant states. These density matrices correspond to system of the same size but with different particle numbers. Thus, at each step of the infinite scheme, the half-block reduced density matrices are formed in the following way:

$$\rho_{L/R} = \mathrm{Tr}_{R/L}\left(\omega_0|\psi(0)\rangle\langle\psi(0)| + \sum_{j=1}^r \omega_j|\psi_j\rangle\langle\psi_j|\right)$$

$$= \mathrm{Tr}_{R/L}\left(\omega_0|\psi(0)\rangle\langle\psi(0)| + \omega_{gs}^0|\psi_{gs}^0\rangle\langle\psi_{gs}^0| + \sum_{j=2}^r \omega_j|\psi_j\rangle\langle\psi_j|\right), \tag{6}$$

where $|\psi(0)\rangle$ is the initial state with weight ω_0, $|\psi_j\rangle$ is the jth relevant state having weight ω_j, and $(\omega_0 + \Sigma_{j=1}^r \omega_j = 1)$ and the number of relevant states including the neutral ground state is r. Other states which can be considered as relevant target states are the ground state of the ion, especially in case of inhomogeneous systems. From our earlier studies on the LXW algorithm we have found that for systems such as $(CN)_x$ and $(PN)_x$ consisting of more than one type of atom, it is necessary to target the corresponding cationic ($|\psi_{gs}^+\rangle$) or anionic ($|\psi_{gs}^-\rangle$) ground states also, in addition to the initial wave packet and neutral ground state. Thus, in this case the density matrix is given by

$$\rho_{L/R} = \mathrm{Tr}_{R/L}(\omega_0|\psi(0)\rangle\langle\psi(0)| + \omega_{gs}^0|\psi_{gs}^0\rangle\langle\psi_{gs}^0| + \omega_{gs}^+|\psi_{gs}^+\rangle\langle\psi_{gs}^+\rangle). \tag{7}$$

An exhaustive analysis of the dependence of the charge densities and spin densities of the initial wave packet on the weights of the target states showed that the nature of the initial state does is not very sensitive to the weights. Hence, as in the LXW scheme, we have chosen $\omega_0 = 0.8$ and $\omega_{gs}^0 = \omega_{gs}^+ = 0.1$ for all the systems we have studied.

The initial state for the final lattice, which is obtained using the infinite DMRG scheme, is numerically evolved in time using the time-dependent Schrödinger equation (TDSE). The purpose of this time evolution is to obtain a set of time-dependent states, with which the initial Hilbert space of the time-evolving wave packet can be constructed for starting the finite DMRG scheme. The TDSE has been solved numerically using the second-order multistep differencing scheme (MSD2).[25] We settled on this scheme after trying more accurate schemes such as fourth- and sixth-order
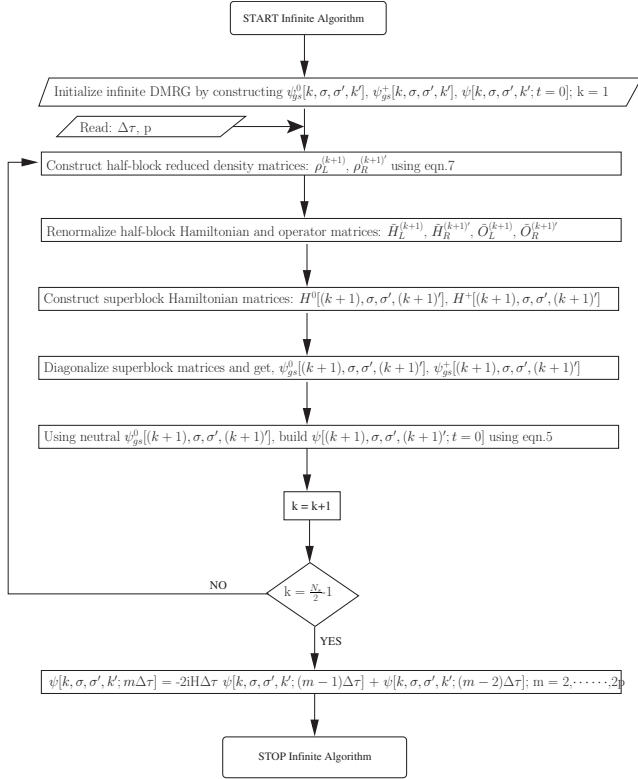
FIG. 2. Flowchart for the infinite DMRG algorithm in the DTWT technique. $k = 1, 2, 3, \ldots, (\frac{N_s}{2} - 1)$ is the half-block length; N_s is the total number of sites in the final lattice. σ and σ' are the two new sites added during the infinite DMRG scheme; ψ_{gs}^0 $[(k+1), \sigma, \sigma', (k+1)']$ and $\psi_{gs}^+[(k+1), \sigma, \sigma', (k+1)']$ are the neutral and ionic ground states. $\psi[(k+1), \sigma, \sigma', (k+1)'; m\Delta\tau]$ is the time-evolved wave packet at $t = m\Delta\tau$, obtained using the MSD2 technique.

multistep differencing schemes (MSD4 and MSD6),[26] and the fourth-order R-K method. The final evolution step is the one that needs accurate integration of the TDSE. The MSD2 scheme is given by the following equation:

$$|\psi(t + m\Delta\tau)\rangle = -2i\tilde{H}|\psi(t + [m-1]\Delta\tau)\rangle + |\psi(t + [m-2]\Delta\tau)\rangle$$
$$+ O(\Delta\tau^3);$$
$$m \in [2, 2p]. \tag{8}$$

The Hamiltonians used in the present study are time independent and $\tilde{H} = (H^+ - E_0^+)$, where H^+ is the Hamiltonian of the positively charged system (cation) and E_0^+ is the ground-state eigenvalue of H^+. The flowchart for the initial infinite DMRG procedure is given in Fig. 2.

B. Hilbert-space adaptation and time evolution using finite DMRG scheme

After obtaining the initial wave packet, the neutral and the ionic ground states, and the time-evolved wave packets $|\psi(k\Delta\tau)\rangle$, $k \in [1, 2p]$, using infinite DMRG algorithm (see Fig. 2), for a system of desired size, finite DMRG procedure

is carried out to adaptively construct the Hilbert space of the Hamiltonian and propagate the wave function in time. Each finite DMRG step generates a system configuration having two blocks joined together by two single sites. Two full sweeps of the finite DMRG procedure involves $4(\frac{N_s}{2} - 2)$ steps, N_s being the final system size; we call $(\frac{N_s}{2} - 2)$ finite DMRG steps a half sweep. Hence, two full sweeps imply sweeping from

$$\left(\frac{N_s}{2} - 1, 1, 1, \frac{N_s}{2} - 1\right) \rightarrow \cdots (N_s - 3, 1, 1, 1)$$
$$\rightarrow \cdots \left(\frac{N_s}{2} - 1, 1, 1, \frac{N_s}{2} - 1\right)$$
$$\rightarrow \cdots (1, 1, 1, N_s - 3)$$
$$\rightarrow \cdots \left(\frac{N_s}{2} - 1, 1, 1, \frac{N_s}{2} - 1\right),$$

where the first and last numbers in parenthesis give the number of sites in the left and right blocks, respectively. At every step of the finite DMRG procedure starting from infinite DMRG solution corresponding to the system

$$\left(\frac{N_s}{2} - 1, 1, 1, \frac{N_s}{2} - 1\right),$$

the following operations are performed.

(1) At time $t = 0$, the reduced density matrix for the appropriate (left or right) block is computed using the neutral ground state $|\psi_{gs}^0\rangle$ with an assigned weight ω_{gs}^0, the initial wave packet $|\psi(0)\rangle$ with weight ω_0, the ionic ground state $|\psi_{gs}^+\rangle$ with weight ω_{gs}^+ and all other preliminary time-evolved states $|\psi(k\Delta\tau)\rangle$ $(k = 1, 2, \ldots, 2p)$ with weights ω_k. The total weight is normalized to unity [Eq. (9)],

$$\rho_{L/R} = \text{Tr}_{R/L}\left(\omega_{gs}^0|\psi_{gs}^0\rangle\langle\psi_{gs}^0| + \omega_{gs}^+|\psi_{gs}^+\rangle\langle\psi_{gs}^+| + \omega_0|\psi(0)\rangle\langle\psi(0)| \right.$$
$$\left. + \sum_{k=1}^{2p} \omega_k|\psi(t + k\Delta\tau)\rangle\langle\psi(t + k\Delta\tau)| \right). \tag{9}$$

At other times $(t \neq 0)$, the reduced density matrix for the appropriate (left or right) block is constructed using the initial state, the ionic ground state, and $2p\Delta\tau$ time-dependent states (the neutral ground state is not considered), as given below:

$$\rho_{L/R} = \text{Tr}_{R/L}\left(\omega_{gs}^+|\psi_{gs}^+\rangle\langle\psi_{gs}^+| + \omega_0|\psi(0)\rangle\langle\psi(0)| \right.$$
$$\left. + \sum_{k=1}^{2p} \omega_k|\psi(t + k\Delta\tau)\rangle\langle\psi(t + k\Delta\tau)| \right). \tag{10}$$

The weights ω_{gs}^0, ω_{gs}^+, and ω_0 are adjusted (as in the infinite DMRG scheme used to generate $|\psi(t + k\Delta t)\rangle$, $k = 1, 2, 3, \ldots, 2p$, described in the previous section), after exhaustive analysis. In the case of TST algorithm, the weights of the target states can all be chosen to be equal or unequal. However, in our case we find that equal weightage of all the target states severely deteriorates the results. Our tests have shown that the optimal unequal weights for Eq. (9) are $\omega_0 = 0.7$ and $\omega_{gs}^0 = \omega_{gs}^+ = 0.1$ so that $\omega_k = \frac{(1.0 - \omega_0 - \omega_{gs}^0 - \omega_{gs}^+)}{p} = \frac{0.1}{p}$, $\forall k$. In

case of Eq. (10), the optimal weights are $\omega_0 = 0.8$, $\omega_{gs}^+ = 0.1$, and $\omega_k = \frac{(1.0 - \omega_0 - \omega_{gs}^+)}{p} = \frac{0.1}{p}$, $\forall k$.

(2) The resulting left- or right-block density matrix is diagonalized and the DMEVs corresponding to the double time window, $t \rightarrow (t + 2p\Delta\tau)$ are chosen. Using this DMEVs, the renormalized block Hamiltonians ($\widetilde{H}_{L/R}$) and operators ($\widetilde{O}_{L/R}$) are constructed. Using these renormalized Hamiltonians and operators, the superblock Hamiltonian for the current system configuration with required particle numbers is obtained.

(3) The superblock Hamiltonians for neutral and ionic systems are diagonalized using either the Lanczos,[27] Davidson's,[28] or any other iterative sparse matrix diagonalization algorithm[29] to obtain the ionic and neutral ground states. In case of the time evolution from $t = 0$ to $t = \Delta t$, both the neutral and the ionic ground states are needed while for the subsequent time evolutions ($t \neq 0$), only the ionic ground state is required. This implies that two superblock diagonalizations are needed for the initial time evolution while only one superblock diagonalization for the remaining evolutions, at every finite DMRG step. We have used the Davidson's algorithm for diagonalization of the superblock Hamiltonian.

(4) For time evolution from $t = 0$ to $t = \Delta t \equiv p\Delta\tau$, the initial wave packet is explicitly constructed from the neutral ground state according to Eq. (5). Hence, the neutral ground state is retained as a target state in Eq. (9). For the remaining time evolutions ($t \neq 0$), the initial state is transformed from the old DMEV basis to the current one using White's wave function transformation;[30] therefore the neutral ground state is no longer required.

(5) The initial wave packet and superblock Hamiltonian which are both expressed in the current DMEV basis are used to solve the TDSE numerically using the MSD2 scheme from $t \rightarrow (t + 2\Delta t)$ in time steps of $\Delta\tau$.

(6) After two full sweeps the final configuration $(\frac{N_s}{2} - 1, 1, 1, \frac{N_s}{2} - 1)$ is evolved from $t \rightarrow (t + \Delta t) \equiv (t + p\Delta\tau)$. This is the final (single) time window evolution. This is carried out using the fourth-order R-K method. The fourth-order R-K method propagates $|\psi(t)\rangle$ to $|\psi(t + \Delta\tau)\rangle$ using four vectors $|k_1\rangle$, $|k_2\rangle$, $|k_3\rangle$, and $|k_4\rangle$ defined as

$$|k_1\rangle = -i\Delta\tau\widetilde{H}(t)|\psi(t)\rangle,$$

$$|k_2\rangle = -i\Delta\tau\widetilde{H}\left(t + \frac{\Delta\tau}{2}\right)(|\psi(t)\rangle + 1/2|k_1\rangle),$$

$$|k_3\rangle = -i\Delta\tau\widetilde{H}\left(t + \frac{\Delta\tau}{2}\right)(|\psi(t)\rangle + 1/2|k_2\rangle),$$

$$|k_4\rangle = -i\Delta\tau\widetilde{H}(t + \Delta\tau)(|\psi(t)\rangle + |k_3\rangle). \quad (11)$$

The state at time $(t + \Delta\tau)$ is given by

$$|\psi(t + \Delta\tau)\rangle \approx \frac{1}{6}(|k_1\rangle + 2|k_2\rangle + 2|k_3\rangle + |k_4\rangle) + O(\Delta\tau^5).$$
$$(12)$$

The obtained time-dependent states can be either saved to disk for future use or they can be used on the fly for calcu-

lating dynamical observables. The final state $|\psi(t + p\Delta\tau)\rangle$ is then used as the next initial state and the same procedure is repeated for the next single window time propagation (see Fig. 3).

In the infinite DMRG part of the DTWT technique, the half-block density matrices and the corresponding DMEVs are constructed from the initial wave packet, the neutral ground state, and the ionic ground state, all of which are time-independent real wave functions. Hence in the infinite DMRG part of our algorithm, all operations are performed in real arithmetic and the quantities (scalars, vectors, and matrices) involved, are all real. However, in the finite DMRG part we encounter time-dependent states which are complex quantities, resulting in complex reduced density matrices, DMEV basis, renormalized left- and right-block Hamiltonians, block operators, and superblock Hamiltonian matrices. Therefore, the DTWT method as implemented by us performs real arithmetic for the infinite DMRG part and complex arithmetic for the finite DMRG part.

III. SOME NUMERICAL ISSUES

It is well known in the literature that the sparse superblock matrix diagonalization is the most time-consuming step in both the infinite and finite DMRG schemes. For the time evolution from $t = 0$ to $t = p\Delta\tau$, each step of the finite part of our DTWT algorithm involves two sparse matrix diagonalizations: one for the neutral system's Hamiltonian and the other for the ionic system's Hamiltonian. For all subsequent time evolutions, $t > p\Delta\tau$, diagonalization of only the superblock Hamiltonian for the ionic system is required at each step of the finite part of the DTWT procedure. If the sparse matrix diagonalizations involved at each step of the finite DMRG part of our algorithm can be replaced by the wave-function transformation introduced by White,[30] computational time is substantially reduced. However, our tests indicated that for the finite DMRG steps, $(N_s - 4, 1, 1, 2) \leftrightarrows (N_s - 3, 1, 1, 1)$ and $(2, 1, 1, N_s - 4) \leftrightarrows (1, 1, 1, N_s - 3)$, the wave-function transformation fails to be accurate. Thus, the matrix diagonalization step needs to be selectively replaced by the wave-function transformation. Taking recourse to White's wave-function transformation, we reduce the number of sparse matrix diagonalizations for the initial time evolution $(0 \rightarrow p\Delta\tau)$, from $8(\frac{N_s}{2} - 2)$ to 8 for two full sweeps; for all subsequent time evolutions ($t > p\Delta\tau$), the wave-function transformation reduces the number of superblock Hamiltonian diagonalizations from $4(\frac{N_s}{2} - 2)$ to 4, for (every) two full sweeps, thereby reducing the computational time significantly. Obtaining the ground-state wave function and energy through matrix diagonalization involves the solution of an eigenvalue equation, $(H|\psi_{gs}\rangle = E_{gs}|\psi_{gs}\rangle)$ while obtaining the same using the wave-function transformation involves transformation of the ground state from the old to current DMEV basis, followed by the evaluation of E_{gs} as $E_{gs} = \frac{\langle\psi_{gs}|H|\psi_{gs}\rangle}{\langle\psi_{gs}|\psi_{gs}\rangle}$; H being the superblock Hamiltonian in the current DMEV basis.

As the number of target states used for constructing the reduced block density matrices increases, the overall compu-
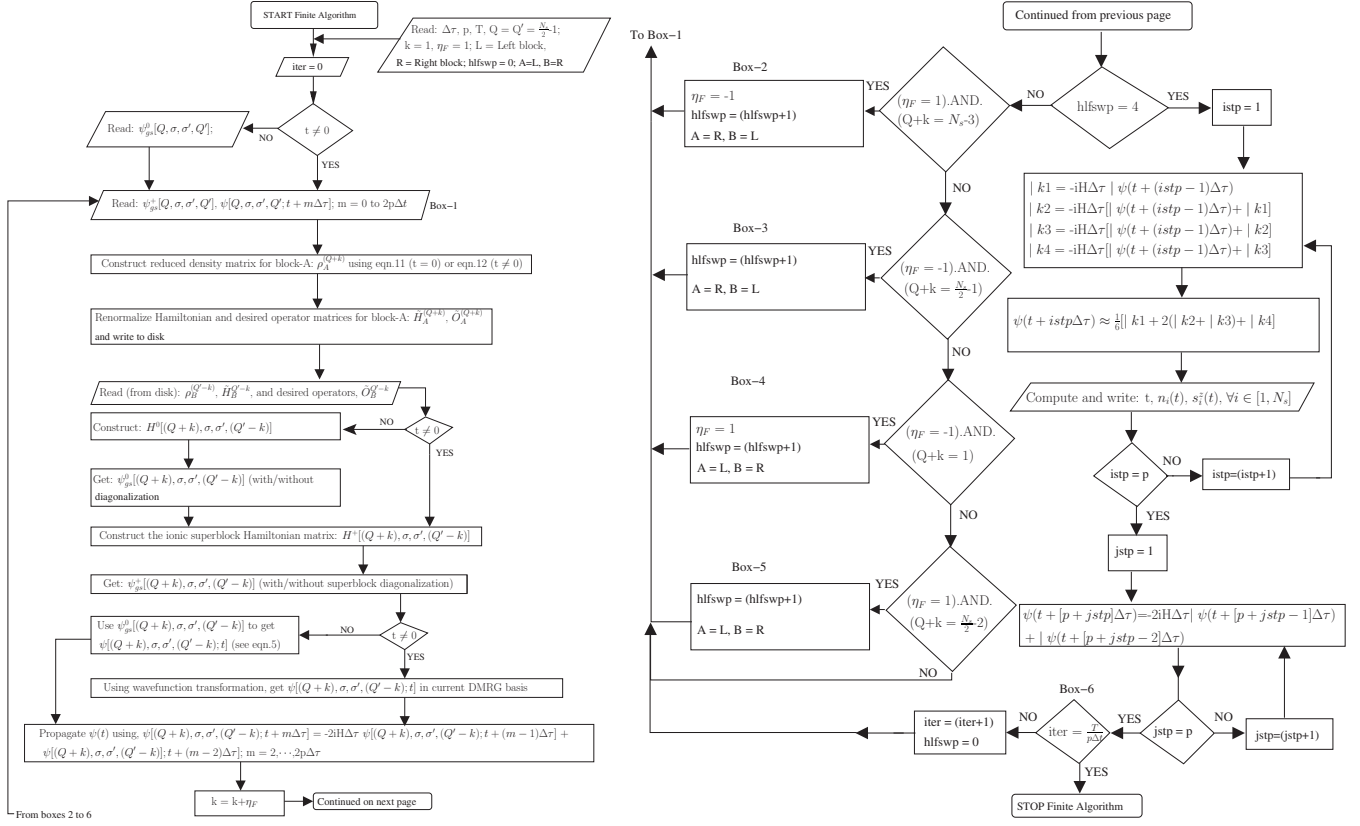
FIG. 3. Basic scheme showing the use of finite DMRG algorithm in the DTWT technique. $Q+k(Q'-k)$ is the length of left (right) block. η_F denotes the direction of sweep: $\eta_F=1(-1)$ implies left(right)$\rightarrow$right(left) sweep. hlfswp=number of half sweeps. Time evolution is performed using fourth-order RK technique while basis adaptation is done using the MSD2 technique.

tational time for the infinite and finite DMRG schemes also increases. The infinite part of DTWT algorithm uses three target states while the finite part needs $2p$ states as target states. Hence, the finite part of our algorithm is slower compared to the infinite part. To overcome this problem, we have used the window modification that we developed and employed in the context of LXW algorithm. Instead of retaining all the $2p$ time-dependent states as target states, we keep $\frac{2p}{10}$ target states; instead of 10, other variations can also be employed. Incorporation of the window modification into the finite part of our algorithm has an interesting consequence, namely, the $2p<m$ condition can be replaced by $\frac{2p}{10}<m$, thereby making it feasible to increase the length of both the double ($2\Delta t$) and single (Δt) time windows.

The time step error associated with the fourth-order R-K technique is $O(\Delta t^5)$ while that associated with the MSD2 scheme is $O(\Delta t^3)$. Thus, the former time propagation scheme is more accurate than the latter. However, the TDSE solver required for constructing the Hilbert space of the time-evolving wave function need not be very accurate compared to TDSE solver needed to propagate the wave packet in time. Hence we have used two different time propagation techniques for the two different windows present in our algorithm. For the double time window ($2\Delta t$) evolution which is used for basis adaptation, we have used the second-order multistep differencing (MSD2) scheme,[25] given by

$$|\psi(t+\Delta\tau)\rangle = -2iH\Delta\tau|\psi(t)\rangle + |\psi(t-\Delta\tau)\rangle, \qquad (13)$$

which uses one sparse matrix-vector multiplication (SMVM) operation for every propagated time step $\Delta\tau$. The two states $|\psi(t)\rangle$ and $|\psi(t-\Delta\tau)\rangle$ are obtained once in the beginning of every time evolution using fourth-order R-K technique. Hence, every time evolution from $t\rightarrow(t+2p\Delta\tau)$ involves $(8+[2p-2])=(2p-6)$ SMVMs. For the final single time window propagation we employ the fourth-order R-K technique as the TDSE solver. Hence, every time evolution from $t\rightarrow(t+p\Delta\tau)$ would require $4p$ SMVMs. Therefore, each single time window propagation using the MSD2 and R-K techniques involves $([2p-6]\times4[\frac{N_s}{2}-2]+4p)$ SMVMs.

IV. COMPARISON OF THE DTWT SCHEME WITH THE LXW AND TST TECHNIQUES

In this section we present a comparative analysis of the computational efficiency of our DTWT scheme with the LXW and TST schemes. In the TST technique, as pointed by White, the wave function is propagated in time after either one or several half sweeps depending on the how many half sweeps are needed to update the Hilbert space of the wave function adequately. Each half sweep (according to our definition of half sweep) needs $(\frac{N_s}{2}-2)$ finite DMRG steps. If the wave function is propagated in time by $\Delta\tau$ after every half
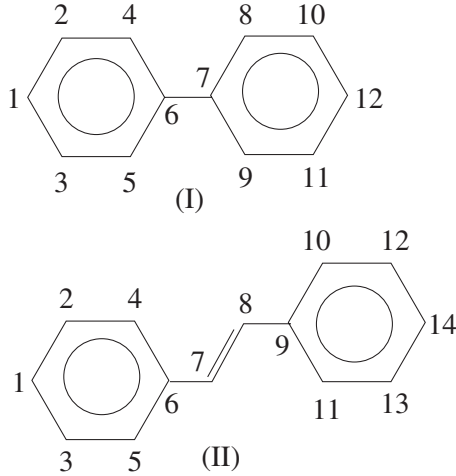
FIG. 4. Molecular structures of (i) biphenyl and (ii) stilbene molecules. Biphenyl and stilbene are the monomers of polyparaphenylene and polyparaphenylvinylene polymers, respectively. Site numbering scheme as employed by us is also shown in the figure.

sweep, then for the total time propagation, $Np(\frac{N_s}{2}-2)$ finite DMRG steps are needed. However, if the wave function is propagated after every q half sweeps, then $Npq(\frac{N_s}{2}-2)$ finite DMRG steps are needed for propagating the initial wave packet over the entire time interval, 0 to T. In the DTWT technique, for every two full sweeps ($q=4$) the wave function is evolved by a time interval Δt which implies that $Nq(\frac{N_s}{2}-2)$ DMRG steps are needed for evolving the initial state over the entire time interval. Therefore, the ratio of DMRG steps in DTWT to TST is either $\frac{4}{pq}$, if $q\neq 1$, or $(4/p)$, if $q=1$ in the TST procedure. Since p is chosen to be $\geq 10^2$, the DTWT scheme is more efficient than the TST technique
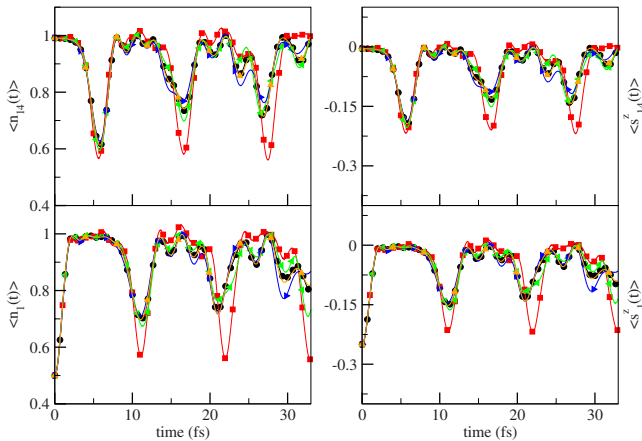

FIG. 5. (Color online) Time evolution profiles of charge (left curve) and spin (right curve) densities at first and last sites of a 14-site Hückel chain, using three different techniques. The color codings for the curves are as follows: black curve with circles =exact; red curve with squares=TST(m=64); green curve with left triangles=TST(m=100); blue curve with right triangles =DTWT(m=64); and orange curve with up triangles=DTWT(m=100). The m=100 DTWT curve is almost indistinguishable from the exact curve. Δt=0.066 fs and $\Delta \tau=\frac{\Delta t}{10}$ are used in the TST technique. In the DTWT scheme, $\Delta \tau$=0.066 fs is employed.
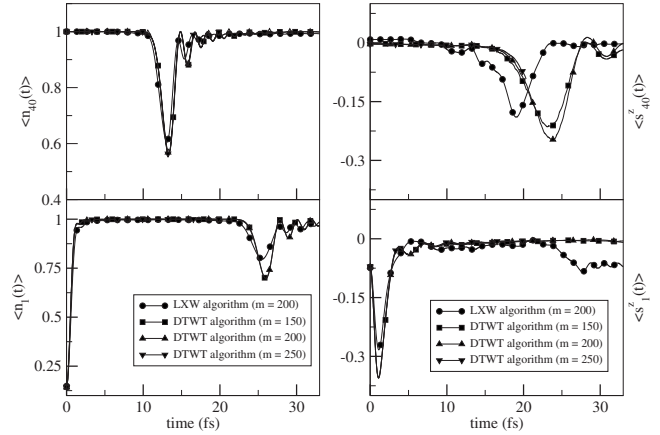

FIG. 6. Comparison of time evolution of charge (left curve) and spin (right) densities at the first and last sites of a 40-site Hubbard chain, using the LXW and DTWT techniques. In both the DTWT and LXW schemes, $\Delta \tau$ is taken to be 0.066 fs.

by a factor of ≥ 25. The actual CPU time involved in the time evolution by the fourth-order R-K procedure is the same in both TST and DTWT schemes. In case of the LXW algorithm, the DMRG steps involved are fewer for a system size N_s, the number of DMRG steps is only $(\frac{N_s}{2}-1)$. However, we evolve the wave packet at each system size and this is the CPU intensive part of the calculation. Besides, the target states in LXW scheme is equal to number of time intervals N (specially for systems with long-range interactions), which is $\sim 10^4$ or more. Therefore the DMEV cutoff required for comparable accuracy is huge ($\sim 10^4$) and unattainable. This leads to large errors in the LXW scheme at long times.

To test the method we compared the DTWT results for various m values with exact time evolution of a 14-site Hückel as well as PPP chain. We also compared these results with those obtained by the TST method for a 14-site Hückel chain and LXW for a 40-site Hubbard chain with $\frac{U}{|t|}=4$. To test whether our DTWT scheme is applicable to other geometries, we have compared the exact time evolution of a 12-site biphenyl molecule and a 14-site stilbene molecule (see Fig. 4), both modeled by the PPP Hamiltonian, with different DMEV cutoffs, m. We have dealt with Hückel chains of length up to 14 sites since the number of states (although known exactly) become too large and the computations become cumbersome for time propagation of the wave packet.

The model Hamiltonians used in this study are the tight-binding Hamiltonian,[31,32] also known as the Hückel Hamiltonian to chemists, the Hubbard[33–35] and PPP Hamiltonian.[36,37] The second-quantized Hamiltonians for these models are give below:[38]

$$H_{\text{Hückel}} = \sum_{\langle ij\rangle,\sigma=\uparrow,\downarrow} t_{ij}(c_{i,\sigma}^{\dagger}c_{j,\sigma} + c_{j,\sigma}^{\dagger}c_{i,\sigma}),$$

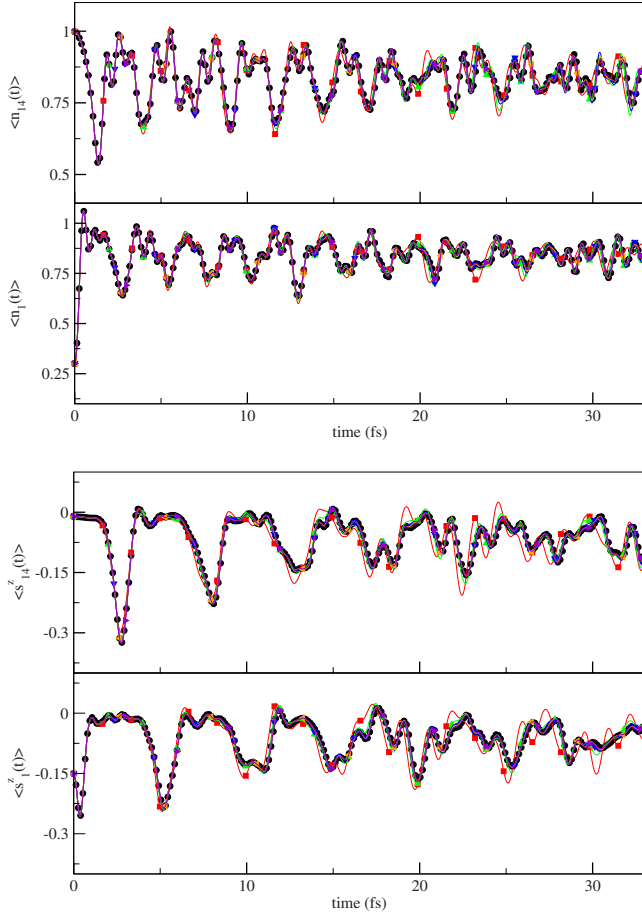$$H_{\text{Hubbard}} = H_{\text{Hückel}} + \sum_i U_i n_{i,\uparrow}n_{i,\downarrow},$$

FIG. 7. (Color online) Comparison of exact versus DTWT time evolution of charge (top curve) and spin (bottom curve) densities at first and last sites of a 14-site PPP chain. $\Delta \tau$ is chosen to be 0.0066 fs. The color coding is as follows: black curve with circles=exact; red curve with squares=DTWT(m=64); green curve with up triangles=DTWT(m=100); blue curve with down triangles =DTWT(m=150); orange curve with left triangles=DTWT(m =200); violet curve with right triangles=DTWT(m=250). It is observed that for $m \gtrsim 100$, the curves converge toward the exact time evolution and for m=200, the DTWT curve is coincident with the exact curve.

$$H_{\text{PPP}} = H_{\text{Hubbard}} + \sum_{i>j} V_{ij}(n_i - z_i)(n_j - z_j). \qquad (14)$$

In the first equation, the summation is restricted to bonded neighbors $\langle ij \rangle$, t_{ij} is the hopping integral between bonded neighbors. U_i is the on-site Coulomb repulsion term (Hubbard U term) of the ith site, $c_{i,\sigma}^{\dagger}$ ($c_{i,\sigma}$) creates (annihilates) an electron with spin σ at (from) the ith site, $n_{i\sigma}$ are the corresponding number operators, $n_i = (n_{i,\sigma} + n_{i,-\sigma})$ is the charge density at site i, V_{ij} is the intersite Coulomb repulsion between lattice sites (i,j), and z_i is the on-site chemical potential of site i. For homogeneous systems, $U_i = U$, and is a measure of the Coulomb repulsion between two electrons of opposite spins occupying the same site. (U/t) characterizes the strength of electron correlations. In case of homogeneous sp^2 carbon systems, all sites are singly occupied for charge neutrality and hence $z_i = 1$, $\forall i$. The intersite electron-electron
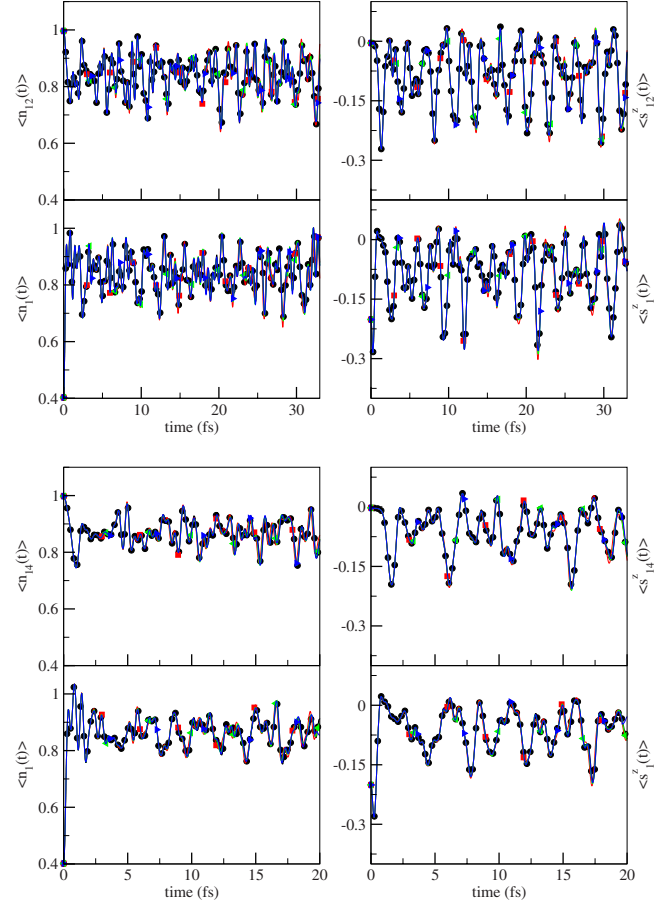
FIG. 8. (Color online) Comparison of exact versus DTWT time evolution of charge (left curve) and spin (right curve) densities at first site and last site of biphenyl system (top) and stilbene molecule (bottom) whose structures are given in Fig. 4. The color coding is as follows: black curve with circles: exact; red curve with squares =DTWT(m=150); green curve with left triangles=DTWT(m =200); and blue curve with right triangles=DTWT(m=250).

repulsion term (V_{ij}) in the PPP model is phenomenologically interpolated between U for zero separation and $\frac{e^2}{r_{ij}}$ for intersite separation $r_{ij} \rightarrow \infty$; thus, the explicit evaluation of the repulsion integrals is avoided. There are two widely used interpolation schemes for evaluating V_{ij}: Ohno scheme[39] and, the Mataga-Nishimoto scheme.[40] In the Ohno interpolation scheme which we use, the V_{ij} term is given by

$$V_{ij} = 14.397 \left[\left(\frac{28.794}{U_i + U_j} \right)^2 + r_{ij}^2 \right]^{-1/2} \qquad (15)$$

and decays more rapidly than the Mataga-Nishimoto formula which is shown below.

$$V_{ij} = \left[\frac{2.0}{U_i + U_j} + \frac{r_{ij}}{14.397} \right]^{-1}. \qquad (16)$$

In both the above interpolation formulas, r_{ij} is measured in angstrom while U and V_{ij} are measured in electron volt. In the Hubbard model calculations, we have used $\frac{U}{|t|}=4$ while in the PPP model we have used standard parameters (U =11.26 eV, t=−2.4 eV, and r=1.397 Å; r being the uni-
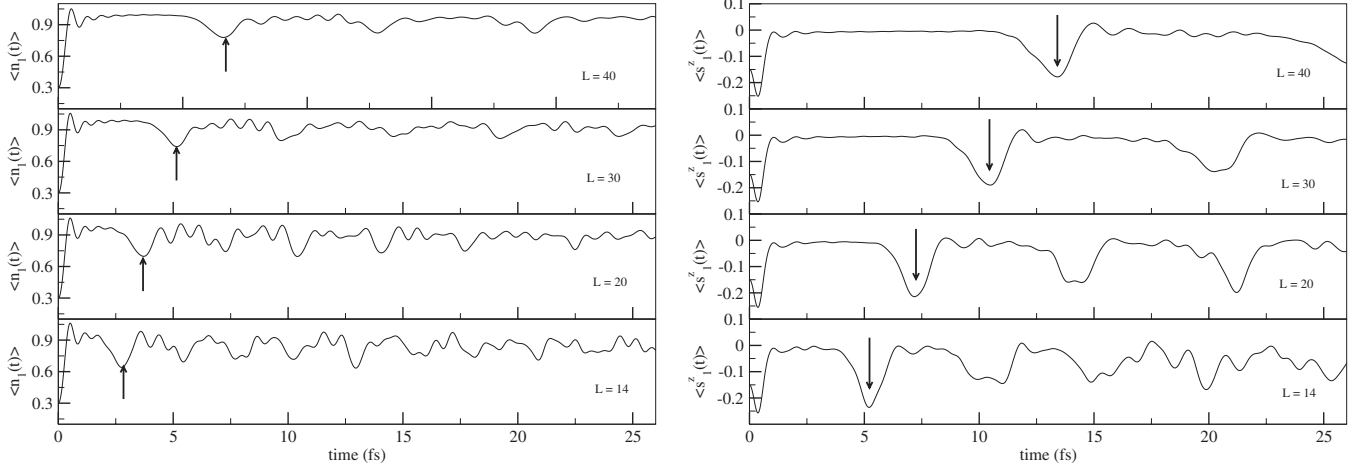
FIG. 9. Time evolution profiles of $\langle n_1(t)\rangle$ (left curve) and $\langle s_1^z(t)\rangle$ (right curve) for regular PPP chains of length 14, 20, 30, and 40. The position of the τ_{2L}^h and τ_{2L}^s are indicated with arrow.

form C-C bond length) and Ohno parametrization.

In Fig. 5 we compare the DTWT and TST schemes for different DMEV cutoffs m for a Hückel chain of 14 sites, with exact results. From Fig. 5 it is clear that for a given system size and m, the DTWT algorithm has a better accuracy than the TST algorithm. The results for the Hubbard chain (Fig. 6) of 40 sites show a smooth convergence in the DTWT scheme as m is increased. This gives confidence in the DTWT scheme. The LXW method with $m=200$ differs from our results quantitatively at long times (Fig. 6). Our results for the 14-site PPP chain indicate that long-range interacting models require higher m for attaining the same convergence as with the nearest-neighbor models (Fig. 7). In Fig. 8 we show the time evolution of the charge and spin densities at the sites numbered according to Fig. 4. Figure 8 also shows that molecular topologies which are not linear require larger DMRG basis dimension to attain accuracies comparable to open chain system.

V. REAL-TIME DYNAMICS OF SPIN-CHARGE SEPARATION IN PPP CHAINS

The quantities we have studied using our time-dependent DMRG algorithm are the time dependence of the site charge and site spin densities. The charge and spin densities at the ith site of a system at time t are, respectively,

$$\langle n_i(t)\rangle = \langle\psi(t)|(n_{i\sigma}+n_{i-\sigma})|\psi(t)\rangle \qquad (17)$$

and

$$\langle s_i^z(t)\rangle = \langle\psi(t)|(n_{i\sigma}-n_{i-\sigma})|\psi(t)\rangle, \qquad (18)$$

where $n_{i\sigma}$'s are the number operators with spin σ and $|\psi(t)\rangle$ is the wave packet evolved in time. Although we have calculated charge (spin) density at all sites of the systems studied in this work, we focus on $\langle n_1(t)\rangle$, $\langle n_L(t)\rangle$, $\langle s_1^z(t)\rangle$, and $\langle s_L^z(t)\rangle$, which suffice to investigate spin-charge separation in the PPP model; 1 and L correspond to the two terminal sites
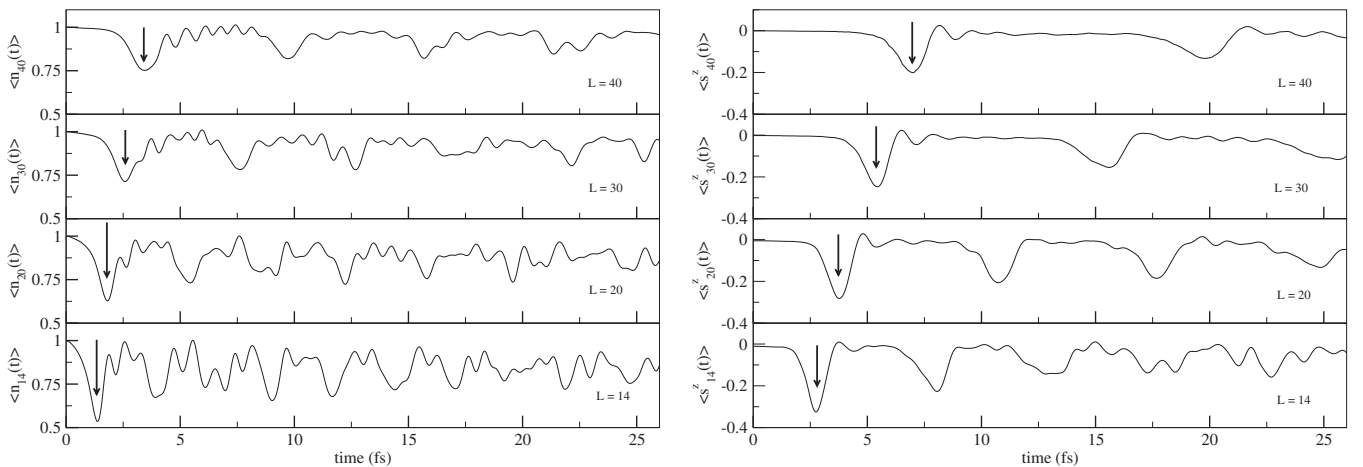

FIG. 10. Time evolution profiles of $\langle n_L(t)\rangle$ (left curve) and $\langle s_L^z(t)\rangle$ (right curve) for regular PPP chains ($L=14,20,30,40$). The position of the τ_L^h and τ_L^s are indicated with arrow.
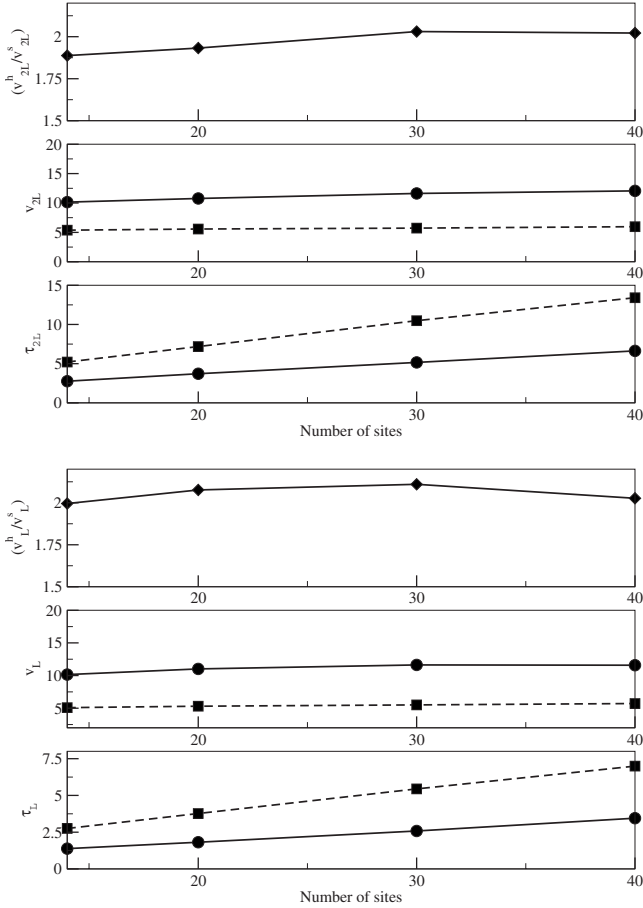
FIG. 11. Variation in $\tau_{L/2L}^{h/s}$ and $\vartheta_{L/2L}^{h/s}$ and the ratio $(\vartheta_{L/2L}^{h} / \vartheta_{L/2L}^{s})$ with chain length in the PPP model. Solid curves with circles represent ϑ_{2L}^{h} (top) and ϑ_{L}^{h} (bottom). Dashed curves with squares represent ϑ_{2L}^{s} (top) and ϑ_{L}^{s} (bottom).

of the chain. We have done two sets of calculations for each of the systems mentioned above, keeping the DMEV basis sizes at 200 and 250, and we find the results converge. Here, we present data obtained with the smaller DMEV basis, namely, with 200 states.

Consider the ground state of a half-filled system with particle density, $n = (\frac{N_e}{2N_s}) = 1/2$, N_e and N_s are, respectively, the total number of electrons and sites in the system. The ground state of this neutral system being an eigenstate of the Hamiltonian is a stationary state. When an electron with a definite spin is either added or removed at a site, from the ground state of the system, a new state forms which is no longer an eigenstate of the governing Hamiltonian. This is a transient (nonstationary) state, popularly known as "wave packet" in the literature, whose time evolution we study for a finite time. In our studies, we annihilate an up-spin electron from site 1 of the systems we have considered and this corresponds to injecting a downspin hole into the system at site 1. In the singlet ($\langle S_{tot}^z \rangle = 0$) ground state of the neutral system, $\langle n_i \rangle \approx 1.0$ and $\langle s_i^z \rangle \approx 0.0$, $\forall i \in [1, N_s]$, N_s = total number of sites in the system. The injected hole at $t = 0$ is localized at the injection site (site 1). In the initial state (wave packet), except at the injection site, all other sites have charge (spin) density of 1.0 (0.0). Evolution of this nonstationary state in

time leads to change in the charge (spin) density distribution of the system, and temporal variation in these dynamical quantities is viewed as propagation of the injected hole from site 1 to site L. Since our systems are not connected to reservoirs, the particle number is fixed and the hole is reflected from the two ends of the system. Hence, time evolution profiles of charge (spin) density consists of a series of small and large maxima and minima. All the systems studied by us are homogeneous, bipartite lattices, implying that all sites are equivalent and the lattice possesses electron-hole symmetry at half filling.

In the absence of electron-electron correlation, temporal variation in charge and spin densities of the injected hole are identical. This is because the charge and spin degrees of freedom of the hole propagate with the same velocity, namely, the Fermi velocity (ϑ_F). Electron-electron correlation decouples these intrinsic degrees of freedom into two separate elementary excitations: holon (carrying charge but no spin) and spinon (carrying spin but no charge). This decoupling is known as spin-charge separation and has been widely studied in the literature. Thus, in the presence of electron-electron correlation, the time evolution profiles of charge and spin densities of the system are different from each other and is recognized as a manifestation of spin-charge decoupling. In order to address the issue of spin-charge separation in the PPP model for a given topology, we have focused on two major extremal points in the time evolution profiles of charge and spin densities of the injected hole. These give us an estimate of the velocity of the charge and spin of the hole, and are therefore helpful in analyzing the spin-charge separation phenomena in the PPP model. These points correspond to the first major minima (dip) in the time evolution profiles of $\langle n_1(t) \rangle$ and $\langle s_1^z(t) \rangle$, and $\langle n_L(t) \rangle$ and $\langle s_L^z(t) \rangle$, respectively, at $t \neq 0$. The time taken for the $t \neq 0$ first minima to appear in the time evolution profiles of $\langle n_1(t) \rangle$ and $\langle s_1^z(t) \rangle$ is associated with the event of the charge and spin degree of freedom of the hole propagating from site 1 to site L and returning to site 1, respectively. The time taken for this dip to appear in the charge (spin) density profile is designated as $\tau_{2L}^h(\tau_{2L}^s)$. The charge velocity deduced from this time is $\vartheta_{2L}^h = (\frac{2L}{\tau_{2L}^h})$ while the spin velocity is $\vartheta_{2L}^s = (\frac{2L}{\tau_{2L}^s})$. The first minima in the temporal profiles of $\langle n_L(t) \rangle (\langle s_L^z(t) \rangle)$ appears when the charge (spin) of the injected hole migrates from site 1 to site L of the system. The time taken for this event is denoted as $\tau_L^h(\tau_L^s)$; charge and spin velocities associated with this event are, $\vartheta_L^h = (\frac{L}{\tau_L^h})$ and $\vartheta_L^s = (\frac{L}{\tau_L^s})$, respectively.

Spin-charge separation in correlated one-dimensional systems has been studied using the DMRG technique by Kollath *et al.*[41] and Ulbricht and Schmitteckert.[42] Kollath *et al.* studied the dynamics of a wave packet obtained by introducing a particle at $t = 0$ in the middle of a long Hubbard chain equilibrated in a spin-dependent site energy acting on the system at time $t < 0$ and turned off at $t = 0$. Both for different fillings and different chain lengths, they observed that the charge and spin velocities were different. Ulbricht and Schmitteckert observed spin-charge separation in a transport simulation involving noninteracting leads and interacting system. The initial wave packet consists of a particle with Gaussian

TABLE I. Variation in τ_L^h, τ_L^s, ϑ_L^h, and ϑ_L^s with chain length, in the Hubbard model with $\frac{U}{|t|}=2.0$, 4.0, 6.0, and the PPP model with $t=-2.4$ eV and $U=11.26$ eV.

Model parameter	L	20	30	40
$\frac{U}{|t|}=2.0$	τ_L^h	6.91679985	9.78119978	12.3353997
	τ_L^s	9.72179978	12.8567997	15.8069996
	ϑ_L^h	2.024057411	2.044738933	3.242699951
	ϑ_L^s	1.44006257	1.55559707	2.53052452
	$(\vartheta_L^h/\vartheta_L^s)$	1.405534352	1.314439949	1.281433918
$\frac{U}{|t|}=4.0$	τ_L^h	7.02239984	10.0517998	13.0811997
	τ_L^s	12.7445997	17.1599996	19.0409996
	ϑ_L^h	5.696058457	5.969080283	6.115647023
	ϑ_L^s	3.138584258	3.496503578	4.201460096
	$(\vartheta_L^h/\vartheta_L^s)$	1.814849623	1.707156921	1.455600406
$\frac{U}{|t|}=6.0$	τ_L^h	7.18739984	10.2827998	12.9755997
	τ_L^s	16.4669996	18.9815996	19.9319996
	ϑ_L^h	2.782647473	2.917493346	3.082709156
	ϑ_L^s	1.214550342	1.580477970	2.006823239
	$(\vartheta_L^h/\vartheta_L^s)$	2.291092742	1.845956351	1.536113942
PPP	τ_L^h	1.81499996	2.58059994	3.45179992
	τ_L^s	3.76859992	5.44499988	6.99599984
	ϑ_L^h	11.019283989	11.625203711	11.588157172
	ϑ_L^s	5.307010674	5.509641995	5.717553018
	$(\vartheta_L^h/\vartheta_L^s)$	2.076363638	2.109974427	2.026768643

probability distribution, moving toward the interacting region, added to one of the leads. The time-dependent study of site spin and charge densities show a separation of spin and charge. Our studies are carried out on molecular systems with long-range interactions and the charge injection is made at the end of the chain.

For studying dynamics in the PPP model, we have considered regular polyene chains (uniform transfer integral). This implies that all bond lengths are equal. Although polyenes are experimentally known to exist in dimerized form, yet our focus being on the algorithm, we have not considered dimerized chains in the present study. Analytical expressions for the velocity of the charge degree of freedom (holon), ϑ_h, and spin degree of freedom (spinon), ϑ_s, in the large U limit of the one-dimensional Hubbard model exist in literature,[43,44]

$$\vartheta_h = 2|t|\sin(\pi n); \quad \vartheta_s = \frac{2\pi|t|^2}{U}\left[1 - \frac{\sin(2\pi n)}{2n}\right], \quad (19)$$

where t and U are, respectively, the nearest-neighbor hopping matrix element and the on-site Coulomb repulsion term, and n is the particle density ($n \leq 1$). From the above expressions it is evinced that while $\vartheta_h \propto |t|$, $\vartheta_s \propto \frac{|t|^2}{U}$. Thus, for a given value of t, increasing U is tantamount to decreasing the velocity of the spinon. Furthermore, as $U \to \infty$, $\vartheta_s \to 0$ and we reach the atomic limit. However, analysis of the charge (ϑ_h) and spin (ϑ_h) velocities of the injected hole for the one-dimensional PPP model do not exist. The PPP model is basically considered as a Hubbard model augmented with an additional long-range Coulomb repulsion term, which leads

to a renormalized U in the Hubbard model. However, the physics of the PPP and Hubbard models are quite different; the potential energy of a configuration not only depends on the number of doubly occupied sites but also on the actual distribution of these sites. Thus, it is not possible to naively map the PPP models to effective Hubbard models. This makes a comparison of the charge and spin velocities of PPP model with those of the Hubbard model interesting. We have carried out this comparison of the PPP results with those of the Hubbard model with $\frac{U}{|t|}=2.0$, 4.0, and 6.0, which we have published previously.[22]

In Figs. 9 and 10 we show the time evolution of $\langle n_1(t)\rangle$, $\langle s_1^z(t)\rangle$ and $\langle n_L(t)\rangle$, $\langle s_L^z(t)\rangle$ for different chain lengths of the PPP model. Time taken for the second minimum to appear in the temporal profiles of $\langle n_1(t)\rangle$ and $\langle s_1^z(t)\rangle$ (Fig. 9) gives τ_{2L}^h and τ_{2L}^s, respectively, and are the time taken by the charge and spin to travel from site 1 to site L and back to site 1. Two observations can be made from the results: $\tau_{2L}^h > \tau_{2L}^s$ for all the chains considered, that is, the hole charge moves faster than the hole spin in the PPP model also, just as in the case of the Hubbard model and the velocities ϑ_{2L}^h and ϑ_{2L}^s are weakly dependent on the system size. Similarly, time taken for appearance of the first minimum in the time evolution profiles of $\langle n_L(t)\rangle$ and $\langle s_L^z(t)\rangle$ (Fig. 10) provides τ_L^h and τ_L^s, respectively. The charge and spin velocities of the hole, ϑ_L^h and ϑ_L^s, calculated from the dynamics of the Lth site as $(\frac{L}{\tau_L^h})$ and $(\frac{L}{\tau_L^s})$, respectively, agree with the velocities calculated from the τ_{2L}^h and τ_{2L}^s values (ϑ_{2L}^h and ϑ_{2L}^s), corresponding to the dynamics of the first site. We also note that finite-size effects are weak from the linear dependence of $\tau_{L/2L}^{h/s}$ on the
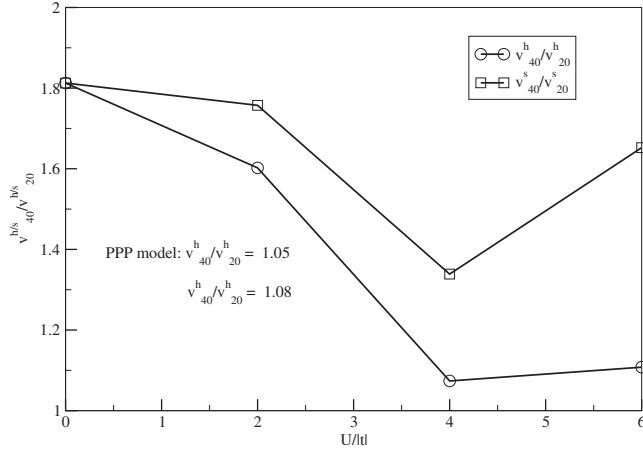
FIG. 12. Finite size effect of hole and spin velocities as a function of correlation strength $\frac{U}{|t|}$. Ratio of the hole (spin) velocity in a 40-site chain to those in a 20-site chain, $\left(\frac{\vartheta_{40}^{h/s}}{\vartheta_{20}^{h/s}}\right)$, is plotted on the Y axis. The ratios for the PPP model are quoted in the figure.

system size and nearly system size independent ratio of $\vartheta_{L/2L}^{h/s}$ (Fig. 11). For the standard PPP parameters, the charge velocity is nearly twice the spin velocity (see Table I). To further investigate the finite-size effects on correlation, we plotted the ratio of hole (spin) velocity for the 40-site chain to that of 20-site chain $\left(\frac{\vartheta_{40}^{h/s}}{\vartheta_{20}^{h/s}}\right)$ versus $\frac{U}{|t|}$ (Fig. 12). In the case of holes it is found that this ratio is maximum for $\frac{U}{|t|}=0.0$ and significantly decreases as $\frac{U}{|t|}$ increases and beyond $\frac{U}{|t|}=4.0$ it is nearly constant, with a value close to 1.0 signifying infinite chain behavior. However, the spin velocity ratio shows a dip at $\frac{U}{|t|}=4.0$ and increases significantly as $\frac{U}{|t|}$ increases. Thus, it appears that the spin properties show stronger finite-size effects than charge properties. In case of the PPP model, it is observed that the ratio of $\left(\frac{\vartheta_{40}^{h}}{\vartheta_{20}^{h}}\right) \approx \left(\frac{\vartheta_{40}^{s}}{\vartheta_{20}^{s}}\right) \approx 1.1$, and the finite-size effects are weak. The finite-size effect in the Hückel model arises from the kinetic-energy term, longer the chain, lower the kinetic energy due to delocalization, and the system is stable. In the Hubbard model, the finite-size effects arise due to suppression of charge fluctuations which is more effective in longer chains due to delocalization. However, in PPP models, the charge fluctuations are better accommodated due to long-range interactions and the kinetic term is not as dominant as noninteracting models. Therefore, we can anticipate weaker finite-size effects in the PPP model than either the Hückel or Hubbard model.

In the extreme case of correlation strength in the Hubbard model $\frac{U}{|t|} \to \infty$, the charge velocity will be a constant near $n \approx 0.5$ and the spin velocity tends to zero [Eq. (19)]. The PPP model therefore appears to be in the intermediate correlation regime. In order to compare the PPP model with the Hubbard model, we have also carried out the time-dependent study for different $\frac{U}{|t|}$ values for the Hubbard model. In Fig. 13 we compare the time evolution of $\langle n_L(t) \rangle$ and $\langle s_L^z(t) \rangle$ of the Hubbard model with $\frac{U}{|t|}=2.0$, 4.0, and 6.0, and the PPP model for different chain lengths. We find that for all the three correlation strengths of the Hubbard model considered, the charge as well as spin, move slower than in the PPP model. The
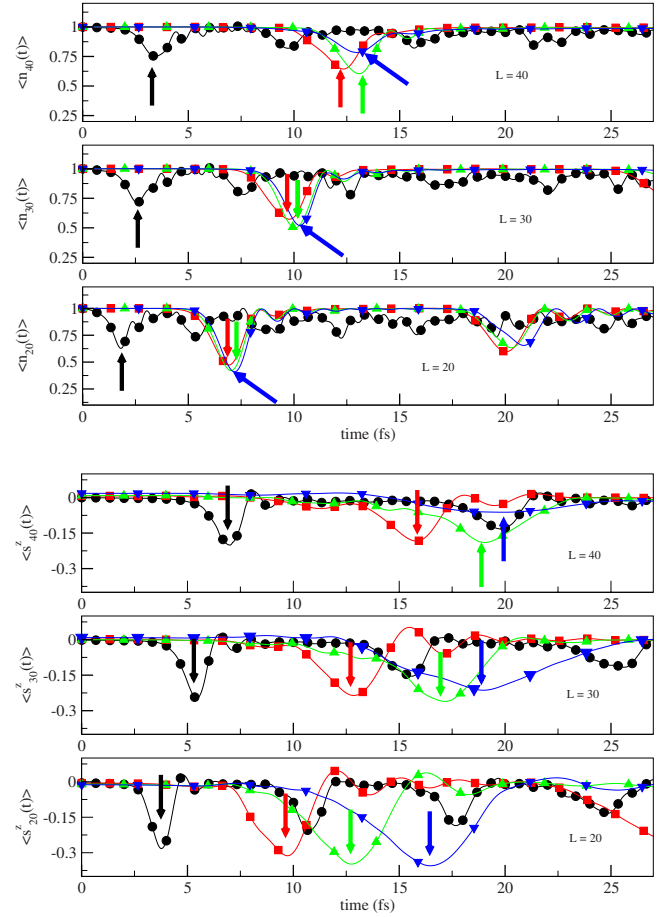

FIG. 13. (Color online) Comparison of the time evolution profiles of $\langle n_L(t) \rangle$ (top curve) and $\langle s_L^z(t) \rangle$ (bottom curve) for regular PPP chains with those of regular Hubbard chains, for chain lengths of 20, 30, and 40 sites. The color coding with symbols is as follows: black curve with circles: PPP model; red curve with squares =Hubbard model with $\frac{U}{|t|}=2.0$; green curve with up triangles =Hubbard model with $\frac{U}{|t|}=4.0$; and blue curve with down triangles=Hubbard model with $\frac{U}{|t|}=6.0$. The position of $\tau_L^{h/s}$ is shown with the aid of arrows: PPP model (black arrow), Hubbard model with $\frac{U}{|t|}=2.0$ (red arrow), 4.0 (green arrow), and 6.0 (blue arrow).

ratio of the charge velocity to the spin velocity for the Hubbard model is presented in Table I. We see that for the Hubbard model with strong correlation strength, $\frac{U}{|t|}=6.0$, this ratio is closer to that of the PPP model. It is usually the practice to compute the effective $\frac{U}{|t|}$ in an extended range model to be $\frac{(U-V_{1,2})}{|t|}$, where $V_{1,2}$ is the first-neighbor electron-electron interaction range. This simplistic interpretation of long-range correlations only renormalizing the U value of the Hubbard model seems to be erroneous in treating the dynamics of doped holes. We note that very strong on-site correlation of $\frac{U}{|t|} > 6.0$ is required to reproduce the ratio of the charge and spin velocities in the PPP model. However, U_{eff} computed as $\frac{(U-V_{1,2})}{|t|}$ for standard parameters is 1.52, underestimates severely the strength of correlations. It appears that the dependence of correlation on energy of the actual charge distribution enhances the role of correlations in the dynamics of charge and spin transport.

VI. SUMMARY AND OUTLOOK

We have developed a time-dependent DMRG scheme called DTWT technique by combining the salient features of the LXW and TST algorithms. This time-dependent DMRG technique is free from the drawbacks associated with both the parent methods while possessing their strengths. Our scheme is faster and more accurate than both the LXW and TST methods. The TST technique targets one time step of length $\Delta\tau$ and evolves the wave packet $|\psi(t)\rangle$ over this time step, using four states constructed over a time interval Δt which is larger than $\Delta\tau$. The time step Δt is used for constructing the Hilbert space representing the time propagating wave packet. However, our studies have revealed that this usually short-time step is unsuitable for representing the Hilbert space of time-evolving system, the reason being, Δt has poor information about the *future* states, along the trajectory of time propagation of the initial wave packet. Hence, the adaptively constructed Hilbert space of the time-evolving wave function fails to follow the evolution successfully. The LXW scheme targets the whole time evolution interval at every system size of the infinite DMRG algorithm. Hence, even though the dimension of DMEV basis (m) is fixed, the adaptively built Hilbert space at every system size successfully follows the time-evolving wave function. However, the DMEV cutoff is significantly less than the number of retained target states. Hence the LXW procedure is capable of constructing the desired Hilbert space successfully. However, the time evolution of the final system is inaccurate due to the fact that number of target states is usually much larger than the DMRG cutoff. Furthermore, the LXW scheme applied to a finite-system size, is not quasiexact. DTWT circumvents these problems efficiently by considering a double time window ($2\Delta t$) for basis adaptation and single time window (Δt) which is embedded within the former time window for evolution. The extra $p\Delta t$ steps within a double time window which are used for targeting ensures that for every single time window propagation, the basis gains the information about the next single time window. This ensures higher accuracy of DTWT technique compared to both the LXW and the TST schemes.

We have found that this method is applicable not only to chains but also to lattices with other topologies like rings and ring-chain systems. Using this technique we have performed nonequilibrium dynamics of spin-charge transport in the PPP model which harbors long-range Coulomb repulsion. Real-time dynamics of spin and charge transport in these systems is still in its infancy in the literature. In future we intend to address the effect of dimerization on the spin-charge separation phenomena as well as, study spin and charge transport in Y junctions. Using our DTWT procedure, we intend to study nonequilibrium transport in a molecule between two leads (having lead-molecule-lead geometry).

Further improvements of the time evolution in the DTWT scheme can be carried out. We recognize that the time-dependent DMRG schemes have two sources of error: (i) the truncation error due to Hilbert-space truncation and (ii) time propagation error due to finite time step employed in the numerical solution of the TDSE. Besides, there is also the problem of stability of the numerical method for time steps larger than a critical value. We intend to overcome the latter two problems by using the Chebyshev polynomial-based decomposition of the time evolution operator. Exact propagation of the wave-packet $|\psi(t)\rangle$ using

$$|\psi(t+\Delta t)\rangle = \sum_{n=1}^{M} c_n e^{-i\Delta t(E_n - E_1)}|\phi_n(t)\rangle, \quad (20)$$

where $|\psi(t)\rangle = \sum_{n=1}^{M} c_n |\phi_n(t)\rangle$, $|\phi_n(t)\rangle$ is the nth eigenstate of H_{DMRG}, E_1 is the ground-state energy, E_n is the nth eigenenergy, M is the order of the matrix H_{DMRG}, and $c_n = \langle \phi_n | \psi(t)\rangle$ has no error associated with solving the TDSE. Chebyshev expansion of the time evolution operator[45,46] has the same advantages as exact expansion of the time evolution operator. The Chebyshev expansion of the state $|\psi(t+\Delta t)\rangle$ is given by

$$|\psi(t+\Delta t)\rangle = e^{-iH\Delta t}|\psi(t)\rangle$$

$$\approx \sum_{n=0}^{M} a_n T_n(\mathbb{H})|\psi(t)\rangle, \quad (21)$$

where $T_n(\mathbb{H})$ is the nth Chebyshev polynomial of the first kind, $\mathbb{H}$ is the scaled Hamiltonian with eigenvalues ranging from $[-1.0, 1.0]$, a_n is coefficient of $T_n(\mathbb{H})$ given by

$$a_n = (2 - \delta_{n0})e^{-i\Delta t[(E_{\max}+E_{\min})/2]}(-i)^n J_n\left(\Delta t \frac{E_{\max} - E_{\min}}{2}\right). \quad (22)$$

$E_{\min}$ and $E_{\max}$ are the minimum and maximum energies of H; J_n is the nth order Bessel function of the first kind. The Chebyshev expansion of the evolution operator can be evaluated up to machine accuracy and there will be no error associated with this time propagation scheme for any arbitrary step size. The use of Chebyshev polynomial expansion scheme is expected to render the DTWT technique free from any time step error besides decreasing the computational time.

*tirthankar@sscu.iisc.ernet.in

†ramasesh@sscu.iisc.ernet.in

[1] A. Dodabalapur, L. Torsi, and H. E. Katz, Science **268**, 270 (1995).

[2] A. Dodabalapur, H. E. Katz, L. Torsi, and R. C. Haddon, Science **269**, 1560 (1995).

[3] J. H. Burroughes, D. D. C. Bradeley, A. R. Brown, R. N. Marks, K. Machey, R. H. Friend, P. L. Burns, and A. B. Holmes, Nature (London) **347**, 539 (1990).

[4] A. Nitzan and M. A. Ratner, Science **300**, 1384 (2003).

[5] S. R. White, Phys. Rev. Lett. **69**, 2863 (1992); Phys. Rev. B **48**, 10345 (1993).

[6] *Density Matrix Renormalization*, edited by I. Peschel, X. Wang, K. Hallberg, and M. Kaulke (Springer, New York, 1999).

[7] S. Ramasesha and Z. G. Soos, Chem. Phys. Lett. **153**, 171 (1988).

[8] Z. G. Soos and S. Ramasesha, J. Chem. Phys. **90**, 1067 (1989).

[9] S. Ramasesha, Z. Shuai, and J. Brédas, Chem. Phys. Lett. **245**, 224 (1995).

[10] S. K. Pati, S. Ramasesha, Z. Shuai, and J. L. Brédas, Phys. Rev. B **59**, 14827 (1999).

[11] K. A. Hallberg, Phys. Rev. B **52**, R9827 (1995).

[12] T. D. Kühner and S. R. White, Phys. Rev. B **60**, 335 (1999).

[13] U. Schollwöck, Rev. Mod. Phys. **77**, 259 (2005).

[14] T. Ulbricht and P. Schmitteckert, EPL **89**, 47001 (2010).

[15] E. Jeckelmann, Phys. Rev. B **66**, 045114 (2002).

[16] H. G. Luo, T. Xiang, and X. Q. Wang, Phys. Rev. Lett. **91**, 049701 (2003).

[17] G. Vidal, Phys. Rev. Lett. **91**, 147902 (2003); **93**, 040502 (2004).

[18] A. J. Daley, C. Kollath, U. Schollwöck, and G. Vidal, J. Stat. Mech.: Theory Exp. (**2004**) P04005.

[19] S. R. White and A. E. Feiguin, Phys. Rev. Lett. **93**, 076401 (2004).

[20] A. E. Feiguin and S. R. White, Phys. Rev. B **72**, 020404 (2005).

[21] M. A. Cazalilla and J. B. Marston, Phys. Rev. Lett. **88**, 256403 (2002); see also **91**, 049702 (2003).

[22] T. Dutta and S. Ramasesha, Comput. Lett. **3**, 457 (2007).

[23] P. Schmitteckert, Phys. Rev. B **70**, 121302 (2004).

[24] S. Manmana, A. Muramatsu, and R. Noack, *Diagonalization-and Numerical Renormalization-Group-Based Methods for Interacting Quantum Systems*, AIP Conf. Proc. No. 789 (AIP, New York, 2005), pp. 93-163.

[25] A. Askar and A. S. Cakmak, J. Chem. Phys. **68**, 2794 (1978).

[26] T. Iitaka, Phys. Rev. E **49**, 4684 (1994).

[27] C. Lanczos, J. Res. Natl. Bur. Stand. **45**, 255 (1950); **49**, 33 (1952).

[28] E. R. Davidson, J. Comput. Phys. **17**, 87 (1975); Comput. Phys. **7**, 519 (1993); Comput. Phys. Commun. **53**, 49 (1989).

[29] R. Barrett, M. Berry, T. F. Chan, M. Donato, J. Dongarra, V. Eijkhout, R. Pozo, C. Romine, and H. van der Vorst, *Templates for the Solution of Linear Systems: Building Blocks for Iterative Methods* (SIAM, Philadelphia, PA, 1994).

[30] S. White, Phys. Rev. Lett. **77**, 3633 (1996).

[31] E. Hückel, Z. Phys. **70**, 204 (1931); **76**, 628 (1932).

[32] L. Salem, *Molecular Orbital Theory of Conjugated Systems* (Benjamin, New York, 1966).

[33] J. Kanamori, Prog. Theor. Phys. **30**, 275 (1963).

[34] M. C. Gutzwiller, Phys. Rev. Lett. **10**, 159 (1963).

[35] J. Hubbard, Proc. Roy. Soc. London **A276**, 238 (1963).

[36] R. Pariser and R. G. Parr, J. Chem. Phys. **21**, 466 (1953).

[37] J. A. Pople, Trans. Faraday Soc. **49**, 1375 (1953).

[38] Peter Surjan, *Second Quantized Approach to Quantum Chemistry* (Springer-Verlag, Berlin, 1989).

[39] K. Ohno, Theor. Chim. Acta **2**, 219 (1964); G. Klopman, J. Am. Chem. Soc. **86**, 4550 (1964).

[40] N. Mataga and K. Nishimoto, Z. Phys. Chem. **13**, 140 (1957).

[41] C. Kollath, U. Schollwöck, and W. Zwerger, Phys. Rev. Lett. **95**, 176401 (2005).

[42] T. Ulbricht and P. Schmitteckert, EPL **86**, 57006 (2009).

[43] E. A. Jagla, K. Hallberg, and C. A. Balseiro, Phys. Rev. B **47**, 5849 (1993).

[44] C. F. Coll, Phys. Rev. B **9**, 2150 (1974).

[45] H. Tal-Ezer and R. Kosloff, J. Chem. Phys. **81**, 3967 (1984), and references therein.

[46] C. Lubich, *From: Quantum to Classical Molecular Dynamics: Reduced Models and Numerical Analysis*, Zurich Lectures in Advanced Mathematics Vol. 12 (European Mathematical Society, ETH-Zurich, Switzerland, 2008).